FULL-FIELD MEASUREMENTS OF SELF-EXCITED OSCILLATIONS IN MOMENTUM-DOMINATED HELIUM JETS

B.S. Yildirim and A.K. Agrawal*
School of Aerospace and Mechanical Engineering,
University of Oklahoma
Norman, Oklahoma 73019

ABSTRACT

Flow structure of momentum-dominated helium jets discharged vertically into ambient air was investigated using a high-speed rainbow schlieren deflectometry (RSD) apparatus operated at up to 2000 Hz. The operating parameters, i.e., Reynolds number and Richardson number were varied independently to examine the self-excited, flow oscillatory behavior over a range of experimental conditions. Measurements revealed highly periodic oscillations in the laminar region at a unique frequency as well as high regularity in the flow transition and initial turbulent regions. The buoyancy was shown to affect the oscillation frequency and the distance from the jet exit to the flow transition plane. Instantaneous helium concentration contours across the field of view revealed changes in the jet flow structure and the evolution of the vortical structures during an oscillation cycle. A cross-correlation technique was applied to track the vortices and to find their convection velocity. Time-traces of helium concentration at different axial locations provided detailed information about the oscillating flow.

* Corresponding Author
Associate Professor
865 Asp Avenue, Room 208
School of Aerospace and Mechanical Engineering
University of Oklahoma, Norman, OK 73019
Phone: (405) 325-1754, Fax: (405) 325-1088, email: aagrawal@ou.edu

1. Introduction

Flow structure and instability of gas jets has been the subject of several investigations in the past. When a low-density gas jet is injected into a high density environment, self-excited, highly periodic oscillations occur in the flow field under some conditions. Even in transition and turbulent flow regimes, large scale structures behave in a repetitive coherence. Several studies have been conducted to characterize the instability and its effects on the flow structure. The important parameters in these studies are the jet Reynolds number ($\mathrm{Re} = U_j d / \nu$ where U_j is the mean jet exit velocity, d is the jet exit diameter, and ν is the kinematic viscosity), the jet Richardson number ($Ri = g.d.(\rho_\infty - \rho_j)/(\rho_j.U_j^2)$ where g is the gravitational acceleration, ρ_∞ and ρ_j are the free-stream and jet densities, respectively) and the Strouhal number ($St = f.d/U_j$ where f is the flow oscillation frequency). Low-density jets are classified as either buoyancy-dominated (Ri>1.0) or momentum-dominated (Ri<<1.0).

Several researchers have studied self-excited oscillations in buoyancy-dominated jets using helium or helium/air mixture as the low-density fluid. Subbarao and Cantwell (1992) identified the oscillating and non-oscillating regimes for vertical helium jets in a co-flow of air. They reported the oscillating behavior of the helium jet at moderate values of Richardson numbers (0.5<Ri<6.0) and stated that this type of flow was subjected to an unusual type of transition to turbulence, consisting of a rapid but highly structured and repeatable breakdown and intermingling of the jet and free stream fluids. The strong dependence of Strouhal number on Richardson number indicated the dominance of the buoyancy effects. Hamins et al. (1992) used the shadowgraph technique to measure the oscillation frequency of helium jets in quiescent air over a range of Froude number (≈ 0.001 to ≈ 1) and Reynolds number (≈ 1 to ≈ 100). Flow

oscillations were not observed until a minimum jet exit velocity was attained. The Strouhal number correlated with inverse Froude number (or Ri), indicating strong buoyancy dependence. Similar observations in round and planar helium jets were made by Cetegen and Kasper (1996), Cetegen (1997), and Cetegen et al. (1998), who extended the operating regime of Richardson numbers to that in pool fires and buoyant plumes. Although self-excited oscillations in these studies were attributed to buoyancy, the direct physical evidence was provided by experiments of Yep et al. (2003) who found that the flow oscillations observed in Earth gravity vanished in the microgravity environment of the 2.2-sec drop tower.

Self-excited oscillations have also been observed in the momentum-dominated flow regime of low-density gas jets. Using helium and helium/air mixtures, Sreenivasan et al. (1989) found pure oscillations in the near field below a critical density of the jet fluid. Flow visualization revealed intermittent breakdown and spectacular spreading of the low-density jet, beyond a certain axial distance. Monkewitz et al. (1990) reported the spectacular spreading of unstable heated air jets below the critical value of density ratio (jet fluid density/ambient fluid density) of approximately 0.73. The spreading of the jet was characterized by the formation of vortex-ring structures and side-jets. Kyle and Sreenivasan (1993) studied the instability and the subsequent breakdown of axisymmetric jets of helium/air mixtures emerging into the ambient air. The oscillating behavior characterized by Strouhal number was shown to depend upon the density ratio, the jet diameter, and the jet momentum thickness, and it was nearly independent of the jet Reynolds number within the covered range $1500 < Re < 12{,}500$. The high degree of repeatability of the oscillating mode and strong interaction between jet flow and vortices led to large centerline velocity fluctuations. Richards et al. (1996) also found pure helium jets to display the self-excited behavior characterized by intense vortex interaction. Concentration measurements at

several radial locations obtained by an aspirating probe indicated increased mixing caused by the side jets. Global oscillations were reported for Reynolds numbers between 350 and 1850. Raynal et al (1996) observed similar self-excited oscillations in planar low-density helium jets.

While the self-excited oscillations in low-density jets at Ri>1.0 are caused by the buoyancy (Yep et al. 2003), the origin of the instability or oscillations in the momentum-dominated jets (Ri<<1.0) remains unknown. In past studies, the buoyancy was considered negligible in momentum-dominated jets and hence, it was ignored (Sreenivasan et al., 1989; Monkewitz et al., 1990; Kyle and Sreenivasan 1993; Richards et al., 1996). However, buoyancy may be important locally, especially in the jet shear layer where the axial momentum is small. In this study, we seek to study global features of flow oscillations in momentum-dominated helium jets at Ri<0.1 to examine the buoyancy effects by independently varying the two operating parameters, i.e., Reynolds number and Richardson number. The transition from laminar to turbulent flow will be investigated with the emphasis to identify the buoyancy effects. Later, we will present full-field helium concentration measurements to study the dynamics of the oscillating flow field. The diagnostics involves quantitative rainbow schlieren deflectomtery, a non-intrusive, optical technique for scalar measurements in non-reacting (Alammar et al., 1998; Pasumarthi and Agrawal, 2003) and reacting flows (Albers and Agrawal, 1999; Agrawal et al., 2002). Unlike previous applications of the rainbow schlieren technique, the present study utilizes a high-speed digital imaging system, needed to resolve the dynamics of the momentum-dominated low-density jets.

2. Experimental Approach

A compact test rig primarily designed and constructed for experiments in the 2.2-sec drop tower was used in this study. An external flow system was coupled with the test rig to increase the maximum flow rate. The flow system comprised of a high purity grade compressed helium cylinder, a pressure regulator, a needle valve to specify the helium flow rate, a calibrated mass flow meter, flexible plastic hoses and a vertically oriented straight tube to approximate fully-developed laminar flow at the jet exit. The tube outer surface was chambered at 30^0 to reduce its wall thickness to 1.0 mm at the exit.

The optical layout of the rainbow schlieren apparatus is similar to that of Yep et al. (2003), with changes made to achieve acceptable schlieren image quality using the high-speed digital camera. The 150-W halogen light source was integrated with a focusing optics assembly to maximize light collection at the inlet plane of the 600 μm diameter fiber optic cable. The source aperture was 3 mm high and 100 μm wide, the collimating lens was 80 mm diameter and 310 mm focal length achromat, the decollimating lens was 80 mm diameter and 1000 mm focal length achromat, and the symmetric rainbow filter was 3mm wide with hue ranging from 40^0 to 330^0. The rainbow schlieren images were acquired by Redlake Motion Xtra HG-TX high speed camera with a 75 mm focal length lens. For each experiment, 2700 images were taken at 1000 Hz or 2000 Hz depending upon the tube diameter, with the camera exposure time of 298 μs. The acquired images were stored digitally in TIFF format at pixel resolution of 384x512 or 144x512.

The color at a specific pixel location in the schlieren image is quantified by hue, uniquely related to the linear displacement of the light ray at the filter plane (Alammar et al, 1998). This relationship, established by calibrating the rainbow filter, provides angular deflection of light ray from measurement of hue in the color schlieren image. Subsequently, an Abel inversion

algorithm for axisymmetric media is utilized to reconstruct the refractive index field. Finally, the helium concentration field is determined by assuming isothermal flow in an ideal, binary gas system. Further details of the analysis procedure are given by Alammar et al. (1998) and Yep et al. (2003).

The uncertainties in the hue values leads to the uncertainties in the deflection angles, which propagate into the uncertainties in the refractive index and helium concentration. The uncertainty of deflection angle determined from the filter calibration curve was 5.0×10^{-4} degree compared to the maximum deflection angle of 4.0×10^{-2} degree. For a given uncertainty in hue (or deflection angle), the uncertainty in helium concentration increases exponentially as one approaches the jet center. (Alammar et al., 1998). This feature of Abel inversion combined with the small angular deflections in the center region (because of low density gradients) produced only qualitative helium concentration data for $r/d<0.2$ and/or concentration values above 90%. Outside these constraints, the uncertainty in helium concentration was 8% of the value. The uncertainty in the jet exit velocity was ± 0.013 m/s and the corresponding uncertainties in the Reynolds number and Richardson number were less than 1% of the value. The spatial resolution in the schlieren image was 0.18mm. The image blur caused by flow convection during finite exposure is another factor that affects the measurements. Based on the camera exposure time of 298 μm, the image blur for the test cases discussed in detail in this study was between 1 mm and 2 mm.

3. Results and Discussion

In this study, a total of nineteen different experiments were conducted spanning a range of Reynolds number from 350 to 2000 and Richardson number from 0.1 to 1.17×10^{-3}. The operating parameters, i.e., Re and Ri were varied independently using tubes with inside diameter of 10.5 mm, 14.5 mm, and 19.05 mm. Table 1 provides details of the experimental test conditions. In §

3.1, global features of flow oscillations will be discussed. The transition behavior from laminar to turbulent flow will be presented in § 3.2. Next, in § 3.3 we will show the instantaneous contour and time traces of helium concentrations to examine the oscillating flow structure. A cross-correlation technique will be utilized to track the large scale vortical structures.

3.1 Global Features and Flow Oscillations.

Figure 1 shows a typical rainbow schlieren image for Re=1200, Ri=8.58×10^{-3} and d=14.5mm. The image depicts the near field laminar region as well as the downstream turbulent region. Zero displacement of light rays at the jet axis and far away from it produces background hue in the schlieren image corresponding to that at the reference location (center) of the symmetric rainbow filter. Hue other than the background hue is produced by light rays deflected because of the finite density gradients in the media. A distinct advantage of the present schlieren technique is that the measurements of angular deflection of light rays are obtained simultaneously across the whole field without perturbing the flow. The Able inversion of angular deflection data however requires an axisymmetric medium. Thus, the field distributions of helium concentration were obtained only in the axisymmetic laminar flow regime and no concentration data are reported in the transition and turbulent flow regimes.

The jet oscillations were characterized by power spectra at a specific location in the flow field obtained by fast Fourier transform (FFT) of hue values acquired from 2048 consecutive schlieren images. Figure 2 shows the power spectra at a fixed axial location, z/d=1.0, for different radial locations, r/d=0.35, 0.41, and 0.5. Figure 2 reveals a dominant frequency of 234 Hz at all radial locations, suggesting global oscillations in the flow field. The spectral power is maximum at r/d=0.41, which is related to the jet core interacting with the outer vortical structure

as will be discussed later. Figure 3 shows power spectra at a fixed radial location, r/d=0.41, for different axial locations, z/d=0.05, 0.5, and 1.0 in the laminar flow regime. Again, a dominant frequency of 234 Hz is observed at all axial locations. Evidently, the flow oscillates immediately past the jet exit, i.e., z/d=0.05. The increase in the peak power signifies the flow oscillations growing in the streamwise direction.

Results in Figs. 2 and 3 demonstrated global oscillations in the laminar flow field. Moreover, the variations in the maximum spectral power suggested flow oscillation amplitude varying in the flow field. Next, we determined the maximum spectral power at various locations to construct the radial profiles at z/d=0.05, 0.5, and 1.0, shown in Fig. 4. Near the jet exit at z/d=0.05, a single peak in maximum power is observed at r/d=0.5 indicating that the flow oscillations are confined to a narrow region downstream of the tube wall. At z/d=0.5, the maximum power has increased by nearly an order of magnitude because oscillations have become more dominant. The radial profile of maximum power shows two peaks, respectively, at r/d=0.40 and 0.53. The double peak structure is attributed to the toroidal vortex around the jet core at this axial location. The separation distance between the peaks is an indication of the width of the vortex. At z/d=1, the maximum power has increased indicating more intense flow oscillations. The maximum power peaks occur at r/d=0.18 and 0.40 suggesting a greater portion of the jet core is affected by the vortex. The penetration of the vortex into the jet core is indicative of contraction of the jet caused by the buoyant acceleration. This situation is different from constant density jets, wherein the vortical structures contribute towards the radial spreading and growth of the jet.

Similar FFT analysis was performed for each experiment to find the global oscillation frequency listed in Table 1. The measured oscillation frequency ranged between 70 Hz and 813

Hz, which explains the need for the high-speed imaging system used in this study. The oscillation frequency increased with decreasing Richardson number, which limited the smallest Ri that could be probed using the 2000 Hz imaging system. It is instructive to compare our measurements using jet tube with d=19.05 mm to those of Richards et al. (1996) using contoured nozzle of 20 mm inside diameter. According to Fig. 5 the present results compare well with those of Richards et al. (1996), whereby the Strouhal number is nearly independent of the Reynolds number. Figure 5 also plots data obtained by Kyle and Sreenivasan (1993) using a contoured nozzle with d=9.3mm. These results indicate that the Strouhal numbers decrease for the small injector diameter.

A potential drawback of Fig. 5 is that the trend shown may be the combined effect of variations in both Re and Ri because Reynolds number and Richardson number are interdependent. Thus Re and Ri were varied independently during experiments. In Figure 6(a), the Strouhal number is plotted versus Reynolds number for fixed Richardson numbers. Results show that the Strouhal number increases slightly as the Reynolds number is increased. The Strouhal number is also affected by the Richardson number; higher Ri resulted in higher St. Figure 6(b) shows Strouhal number versus Richardson number for fixed Reynolds numbers. Again, St is shown to increase with increase in the Reynolds number and/or Richardson number. The dependence of Strouhal number on Richardson number suggests that buoyancy is important even though the jet flow is momentum-dominated. Results in Fig. 6 do not yield a direct correlation between Strouhal number and Re or Ri. In an effort to correlate experimental data, the oscillation frequency (f) was normalized using the buoyancy time scale or the time for a fluid element to move one jet diameter under the action of buoyancy or $\tau = [\rho_j d / g(\rho_\infty - \rho_j)]^{1/2}$. The normalized oscillation frequency $[f_n = f.\tau]$ correlated with Ri for all Reynolds numbers. Based

on a power law fit, the correlation is expressed as: $f_n = 0.434.Ri^{-0.465}$ with correlation coefficient of 0.963 in the range $1.17x10^{-3} < Ri < 4.4x10^{-2}$. Experimental data from Kyle and Sreenivasan (1993) and Richards et al. (1996) also agreed with this correlation as shown in Fig. 7.

3.2 Transition from Laminar to Turbulent Flow

In the previous section, measurements taken only in the laminar flow regime were presented. In this section, we extended the analysis to the transition from the laminar to turbulent flow. Figure 8 shows power spectra at a fixed radial location, r/=0.41, for different axial locations, z/d=1.5, 2.0, and 2.5. At z/d=1.5, the flow is undergoing the transition from the laminar to turbulent flow as shown by the image in Fig. 1. However, the flow oscillates at a unique frequency of 234 Hz, which is the same in the upstream laminar flow region. At z/d=2.0, the oscillation frequency is still the same, i.e. 234 Hz, even though the flow appears visibly turbulent in Fig. 1. The FFT analysis at other radial locations for z/d=1.5 and 2.0 yielded the same unique oscillation frequency (234 Hz), proving that the periodicity is maintained during the transition from the laminar to turbulent flow. Figure 8 shows that the flow is no longer periodic in the downstream turbulent regime at z/d=2.5, where the large scale vortical structures breakdown to produce a broadband power spectra.

Next, we examined the effect of operating parameters on the flow transition process. Figure 9 shows the color schlieren images obtained at different Reynolds numbers and Richardson numbers. Note that the scale of each image is different because several tube sizes were used for the experiments. In the upper set of schlieren images, the Richardson number is kept constant at $18x10^{-3}$ as the Reynolds number is varied from 510 to 1250. At the smallest Re, the jet is laminar in the field of view. At Re=830, the flow transition occurs near z/d=2.5. Further increase in the

Reynolds number causes the transition plane to move closer to the jet exit. The trend of decreasing normalized flow transition length (i.e., the distance from the jet exit to the transition plane divided by the tube inside diameter) with increasing Reynolds number is consistent with similar observations in low-density gas jet by Subbarao and Cantwell (1992), Takano and Kotani (1978), and Takahashi et al. (1982). In the lower set of schlieren images in Fig. 9, the Reynolds number is fixed at 1200 as the Richardson number is varied from 3.53×10^{-3} to 19×10^{-3}. Figure 9 shows that the normalized flow transition length decreases as the Richardson number increases, which is consistent with similar observations in buoyant low-density jets by Subbarao and Cantwell (1992). The size of the turbulent structures is also affected by the Richardson number; small scale structures are observed at lower Ri while structures are larger at higher Ri. These unexpected results clearly demonstrate that buoyancy affects the flow transition even for small Richardson numbers; a phenomenon ignored in past studies.

Next, a quantitative assessment of the flow transition length was conducted for various test cases in Table 1. In instantaneous schlieren images, the flow transition was marked by the appearance of small-scale structures across the width of the jet. For given test conditions, the location of the transition plane identified from instantaneous schlieren images however fluctuated with time. Thus, transition length was determined using mean and root-mean-square (rms) deflection angle contours obtained from 2730 consecutive schlieren images. Figure 10 shows contours of mean and rms angular deflection for Re=1600 and $Ri=4.83 \times 10^{-3}$. The contours are shown for only one side of the jet axis because of the symmetry. Mean angular deflection contours in Fig. 10(a) show the jet width increasing gradually, making it difficult to accurately identify the transition plane. However, the rms deflection angle contours provide a more direct measure of the transition plane. In the laminar region of the jet, the rms angular deflection was

small and the fluctuations were confined to a narrow shear layer region. Higher rms deflection angle values (on the order of mean deflection angle values) are observed for $z/d \geq 0.9$. Moreover, the rms contours also spread across the width of the jet for $z/d \geq 0.9$, signifying fluctuations caused by the small scale structures. The transition lengths obtained using this approach and measured directly from instantaneous schlieren images were within +/- 0.1d of each other. Figure 11 shows the summarized results of the normalized flow transition length (L/d) versus Richardson number for fixed Reynolds numbers. For a given Reynolds number, the normalized flow transition length decreases as Richardson number increases and the greatest effect of Ri is observed for $Ri<2.0x10^{-2}$. Furthermore, the normalized transition length at a given Richardson number increases as the Reynolds number is decreased. These results clearly demonstrate significant effects of buoyancy on the flow transition in the momentum-dominated low-density gas jets of the present study.

3.3 Full Field Concentration Measurements

Instantaneous Helium Concentration Contours. One of the major advantages of the rainbow schlieren technique is that the concentration measurements are obtained instantaneously across the whole field of view. Figure 12 shows contours of helium molar percentage during an oscillation cycle for Re=800, $Ri=4.4x10^{-2}$, and d=19.05 mm Results show that the helium concentration is changing throughout the cycle because of the instability of the flow field. The flow oscillation period is 9 ms because the contours at t=0 ms and t=9 ms are nearly identical. The FFT analysis for this case indicated flow oscillation frequency of 109 Hz, which matches with the oscillation period of 9 ms. Contours in Fig. 12 reveal features similar to those observed by Pasumarthi and Agrawal (2003) in buoyant helium jets. The curvature of the 80%

concentration contour at t=0 ms in Fig. 12 indicates that the jet contracts near the exit (z/d<0.5), expands in the mid region (<0.5 z/d < 1.0) and contracts again in the downstream region (z/d > 1.0). The contraction of the jet near the exit is attributed to the buoyant acceleration of the low-density fluid in the jet shear layer. Buoyant acceleration entrains the surrounding fluid to eventually produce a toroidal vortex around the jet core. For example, the contraction of the jet producing sharp concave curvature in the 80% concentration contour at t=2 ms signifies the presence of the vortex around z/d=0.65. This explanation is consistent with experimental observations of Cetegen and Kasper (1996) and computational fluid dynamic analysis of Satti et al (2004) in buoyant helium jets. During subsequent phases of the oscillation cycle, the region of concave curvature signifying the vortex propagates in the streamwise direction. In the meantime, the jet expands near the exit during t=4 ms to 7 ms. Subsequently at t=8 ms, the vortex has moved outside the field of view as the jet begins to contract near the exit to produce another vortex and hence, to sustain the oscillations.

Tracking Vortical Structures. The movement of the vortex was tracked using cross-correlation of consecutive pairs of schlieren images (Ben-Yaker and Hanson, 2002). A large scale structure was defined within a specified window of the first image using hue as the parameter. In the second image, a window was specified, where the structure predefined in the first image will be located. The cross-correlation between the two images was calculated at each pixel location of the second image window. The highest cross-correlation magnitude corresponds to the location of the predefined structure in the second image. Details of the procedure to efficiently calculate the cross-correlation magnitudes are discussed by Ben-Yaker and Hanson (2002).. Figure 13 plots the vortex convection velocity obtained by dividing the displacement of vortical structures between consecutive images by the time interval between images. Results

were obtained by tracking vortices for three oscillation cycles to ascertain the cycle to cycle variations. Figure 13 shows that the vortex convection velocity normalized by the average jet exit velocity (V-n) is about 0.4 for axial locations up to z/d=0.75. Subsequently, the vortex gains momentum from the jet core undergoing buoyant acceleration. As a result, the normalized vortex convection velocity increases to 0.7 at z/d=1.5. The vortex convection velocity is nearly the same for each oscillation cycle. These results suggest that the buoyancy is important in the formation and convection of vortical structures affecting the flow oscillations.

Time-Traces of Helium Concentration. One of the effective ways to visualize flow oscillations is by time-traces of helium concentration at a specified axial plane. In addition to monitoring the variations in the radial direction, it is also possible to examine the concentration fluctuations at a fixed radial location. Figure 14 shows time traces of helium mole fraction on one side of the jet centerline for 0.05 sec interval at z/d=0.05, 0.5, 1.0, and 2.0. Plots in Fig. 14 reveal that the flow repeats itself in time indicating an oscillatory mode. Based on the time interval between consecutive peaks (or valleys), an oscillation frequency of 109 Hz was found at all locations, which agrees with the frequency obtained from the FFT analysis. Near the jet exit at z/d=0.05, the concentration fluctuations are small. The helium concentration changes from 80% at r/d=0.45 to 10% at r/d=0.6, indicating a steep gradients in the radial direction. At z/d=0.5, diffusion of helium in the radial direction is observed by noting the helium concentration level of 10% at r/d=0.7. The concentration fluctuations have grown to a noticeable level and the oscillations are highly repeatable from cycle to cycle. The oscillations are most significant in the region between r/d=0.45 and r/d=0.60 with spatial amplitude on the order of 0.05d. For example, the 80% concentration curve fluctuates between r/d=0.45 and r/d=0.50. At z/d=1.0, the jet has expanded radially with 10% concentration level located at r/d=0.78. The

oscillation amplitude has increased at all radial locations. For example, the 80% concentration level resides between r/d=0.42 and r/d=0.53 which signifies near doubling of the spatial amplitude. The large oscillation amplitude signifies greater penetration of the surrounding fluid into the jet core at this axial plane. Further downstream at z/d=2.0, the jet has expanded radially with 10% concentration level located at r/d=0.87. The 80% concentration level fluctuates between r/d=0.30 and r/d=0.52, indicating that the spatial amplitude of oscillations has doubled again. Intense flow oscillations are accompanied with greater penetration of the surrounding fluid into the jet core. Figure 14 reveals time lag between concentration peaks (or valleys) at different axial locations associated with the passage of the vortex.

Effect of Operating Parameters. Figure 15 shows concentration contours during an oscillation cycle for Re=1200 and Ri=1.9×10^{-2}, d=19.05 mm. Again, the flow structure changes throughout the cycle because of the global instability mode. The oscillation period of about 6 ms corroborates with the oscillation frequency of 172 Hz determined from the FFT analysis. Figure 15 shows smaller curvature in concentration contours compared to the previous case (see Fig. 12). Figure 16 shows the corresponding time traces of helium concentration at axial planes, z/d=0.05, 0.5, 1.0, and 1.5. The trends observed in Fig. 16 are similar to those in the previous case (see Fig. 14), i.e., the jet width and oscillation amplitude increase in the axial direction. Moreover, the surrounding fluid penetrates deeper into the jet core at downstream locations.

For the above test case, the flow transition was visible in the field of view of the schlieren image. Thus, we applied the cross-correlation technique to track a large-scale structure passing through the transition/turbulent region. Figure 17 traces the path of a large-scale structure for four consecutive cycles. Unlike the laminar flow regime, the movement of the structure was observed in both axial and radial directions indicating radial spreading of the jet in the turbulent

flow regime. Nearly identical path during consecutive cycles suggests highly repeatable structures passing into the turbulent region. This coherence of flow structures confirms the results of the FFT analysis, showing a unique oscillation frequency in transition and initial turbulent flow regimes.

4. Conclusions

Rainbow schlieren deflectometry technique combined with high-speed digital imaging was applied to study self-excited oscillations in the momentum-dominated helium jets at Richardson numbers between 1.17×10^{-3} and 0.1. Results show global oscillations at a pure frequency in the laminar, transitional, and initial turbulent regions of the jet. The oscillation frequency normalized using the buoyancy time scale correlated with the Richardson number, suggesting that the flow oscillations were buoyancy-induced. The transition from the laminar to turbulent flow was also affected by the buoyancy. For a given Reynolds number, the length scales of turbulent structures were determined by the buoyancy-induced vortices in the upstream laminar regime. Instantaneous helium concentration contours revealed buoyancy-induced jet contraction producing highly periodic vortical structures during an oscillation cycle. The vortical structures were shown to accelerate as they convected downstream while maintaining their periodicity in the transitional and initial turbulent flow regimes. Time traces of helium concentration revealed that the flow oscillation amplitude and penetration of surrounding fluid into the jet core increased in the flow direction.

Acknowledgments

This work was supported by the Physical Sciences Division of NASA's Office of Biological and Physical research under grant NAG 3-2388.

References

Agrawal AK, Alammar KN, Gollahalli SR (2002) Application of rainbow schlieren deflectometry to measure temperature and oxygen concentration in a laminar gas-jet diffusion flame, Exp Fluids 32:689-691

Alammar K, Agrawal AK, Gollahalli SR, Griffin D (1998) Application of rainbow schlieren deflectometry for concentration measurements in an axisymmetric helium jet, Exp Fluids 25:89-95

Albers B, Agrawal AK (1999) Schlieren analysis of flicker in an oscillating gas-jet diffusion flame, Combust Flame 119:84-94

Ben-Yaker A, Hanson RK (2002) Ultra-fast framing schlieren system for studies of the time evolution of jets in supersonic coflows, Exp Fluids 32:652-666.

Cetegen BM, Kasper KD (1996) Experiments on the oscillatory behavior of buoyant plumes of helium and helium-air mixtures, Phys Fluids 8:2974-2984

Cetegen BM (1997) Measurements of instantaneous velocity field of a non-reacting pulsating buoyant plume by particle image velocimetry, Combust Sci Tech 123:377-387.

Cetegen BM, Dong Y, Soteriou MC (1998) Experiments on stability and oscillatory behavior of planar buoyant plumes, Phys Fluids 10:1-7.

Hamins A, Yang JC, Kashiwagi T (1992) An experimental investigation of the pulsation frequency of flames, Proc. Combust Inst 24:1695-1705

Kyle DM, Sreenivasan KR (1993) The stability and breakdown of a round variable density jet, Journal of Fluid Mech. 249:619-664

Monkewitz PA, Bechert DW, Bariskow B, Lehmann B (1990) Self-excited oscillations and mixing in a heated round jet, Journal of Fluid Mech 213:611-639

Pasumarthi KS, Agrawal AK (2003) Schlieren measurements and analysis of concentration field in self-excited helium jets, Phys Fluids 15:3683-3692

Raynal L, Harion JL, Favre-Marinet M, Binder G (1996) The oscillatory instability of plane variable-density jets, Phys Fluids 8:993-1006

Richards CD, Breuel BD, Clark RP, Troutt TR (1996) Concentration measurements in a self-excited jet, Exp Fluids 21:103-109

Satti RP, Pasumarthi KS, Agrawal AK (2004) Numerical simulations of buoyancy effects in low density gas jets, AIAA Paper 2004-1317

Screenivasan, KR, Raghu S, Kyle D (1989) Absolute instability in variable density round jets, Exp Fluids 7:309-317

Subbarao ER, Cantwell BJ (1992) Investigation of a co-flowing buoyant jet: experiments on the effect of Reynolds number and Richardson number, Journal Fluid Mech 245:69-90

Takahashi F, Mizomoto M, Ikai S (1982) Transition from laminar to turbulent free jet diffusion flames, Combust Flame 48:85-95

Takeno T, Kotani Y (1978) Transition and structure of turbulent jet diffusion flames, Prog Astronautics and Aeronautics, AIAA Inc., New York, 58:19-35.

Yep TW, Agrawal AK, Griffin DW (2003) Gravitational effects on near-field flow structure of low-density gas jets, AIAA Journal 41:1973-1979

LIST OF FIGURES

Figure 1. A typical rainbow schlieren image for Re=1200, Ri=8.58x10^{-3}, and d=14.5mm

Figure 2. Power spectra in the laminar flow regime at z/d=1.0 for Re=1200, Ri=8.58x10^{-3}, and d=14.5mm

Figure 3. Power spectra in the laminar flow regime at r/d=0.41 for Re=1200, Ri=8.58x10^{-3}, and d=14.5mm

Figure 4. Maximum spectral power at r/d=0.41 for Re=1200, Ri=8.58x10^{-3}, and d=14.5mm

Figure 5. Strouhal number versus Reynolds number for a fixed tube diameter

Figure 6. (a) Strouhal number versus Reynolds number (b) Strouhal number versus Reynolds number

Figure 7. Flow oscillation frequency versus Richardson number for fixed Reynolds numbers

Figure 8. Power spectra in the transitional/turbulent flow regime at r/d=0.41 for Re=1200, Ri=8.58x10^{-3}, and d=14.5mm

Figure 9. Effect of Reynolds number and Richardson number on transition from laminar to turbulent flow

Figure 10. Mean and rms angular deflection for Re=1600, Ri-4.83x10^{-3}, and d=14.5mm, (a) mean angular deflection (b) rms angular deflection; Contour levels are in milli degrees

Figure 11. Normalized flow transition length versus Richardson number for fixed Reynolds numbers

Figure 12. Instantaneous helium mole percentage contours during an oscillation cycle for Re=800, Ri=4.4x10^{-2}, and d=19.05mm

Figure 13. Vortex convection velocity for Re=800, Ri=4.4x10^{-2}, and d=19.05mm

Figure 14. Time-traces of helium mole percentage at different axial planes for Re=800, Ri=4.4×10^{-2}, and d=19.05mm

Figure 15. Instantaneous helium mole percentage contours during an oscillation cycle for Re=1200, Ri=1.9×10^{-2}, and d=19.05mm

Figure 16. Time-traces of helium mole percentage at different axial planes for Re=1200, Ri=1.9×10^{-2}, and d=19.05mm

Figure 17. Path of a large scale structure in the transitional/turbulent flow regime for Re=1200, Ri=1.9×10^{-2}, and d=19.05mm

Table 1. Experimental test conditions

Test Case	Reynolds Number	Richardson Number	Tube Diameter (mm)	Frequency (Hz)	Strouhal Number
1	800	$44x10^{-3}$	19.05	109	0.41
2	800	$19\ x10^{-3}$	14.5	172	0.37
3	800	$7.33\ x10^{-3}$	10.5	266	0.30
4	1000	$28\ x10^{-3}$	19.05	141	0.42
5	1000	$12\ x10^{-3}$	14.5	203	0.35
6	1000	$4.7\ x10^{-3}$	10.5	391	0.35
7	1200	$19\ x10^{-3}$	19.05	172	0.43
8	1200	$8.58\ x10^{-3}$	14.5	234	0.34
9	1200	$3.53\ x10^{-3}$	10.5	438	0.33
10	1600	$4.83\ x10^{-3}$	10.5	344	0.37
11	1600	$1.83\ x10^{-3}$	14.5	547	0.31
12	2000	$1.17\ x10^{-3}$	10.5	813	0.37
13	530	$100\ x10^{-3}$	19.05	70	0.43
14	350	$100\ x10^{-3}$	14.5	78	0.38
15	910	$34\ x10^{-3}$	19.05	125	0.41
16	605	$34\ x10^{-3}$	14.5	109	0.31
17	1250	$18\ x10^{-3}$	19.05	180	0.43
18	830	$18\ x10^{-3}$	14.5	172	0.36
19	510	$18\ x10^{-3}$	10.5	156	0.28

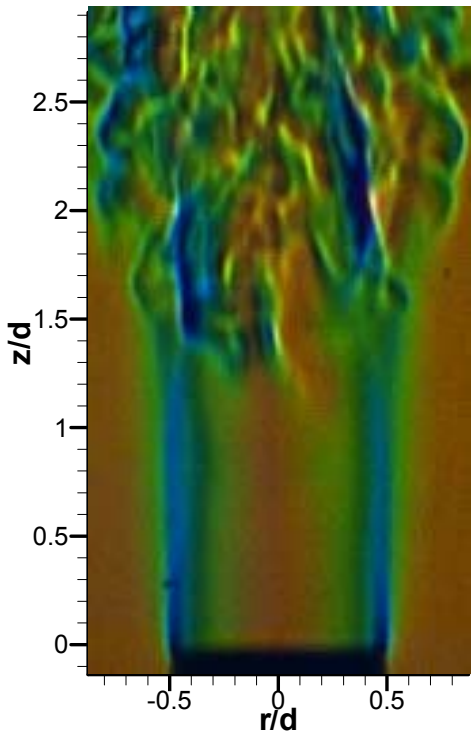

Figure 1. A typical rainbow schlieren image for Re=1200, Ri=8.58×10^{-3}, and d=14.5 mm

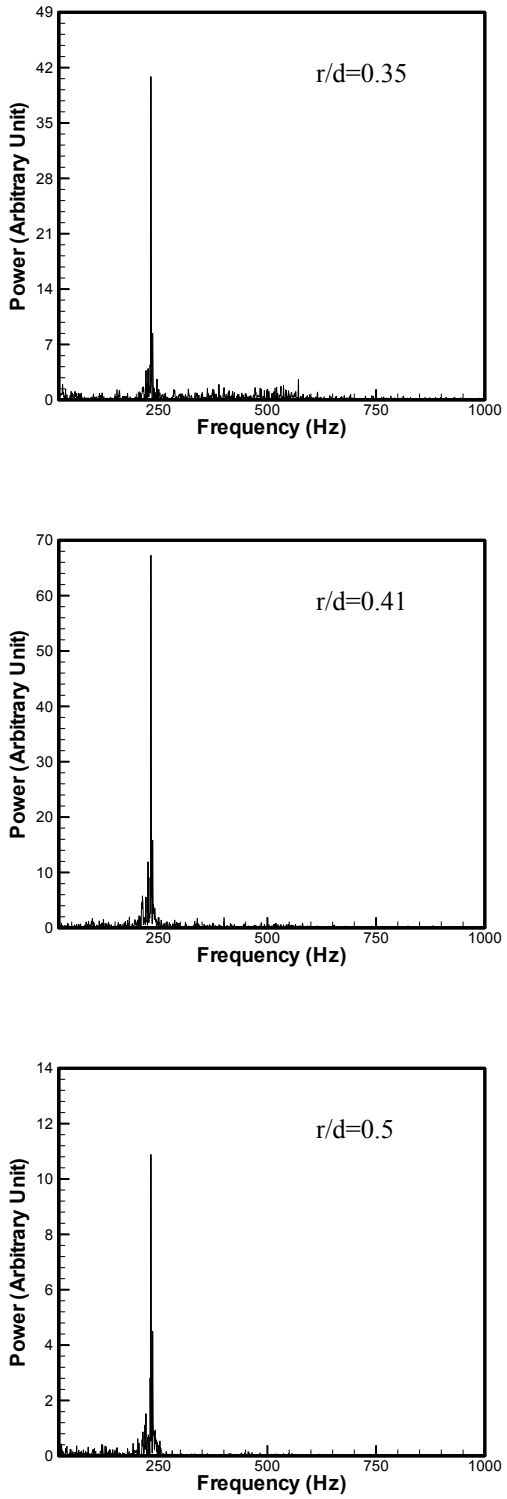

Figure 2. Power spectra in the laminar flow regime at z/d=1.0 for Re=1200, Ri=8.58×10^{-3}, and d=14.5 mm

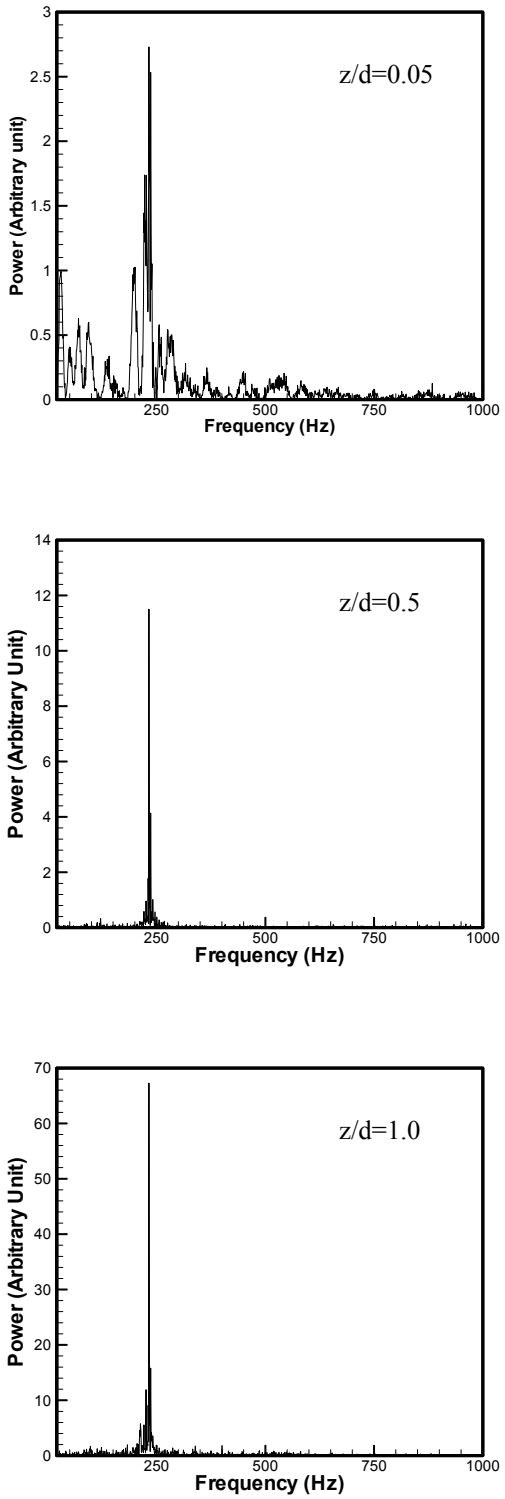

Figure 3. Power spectra in the laminar flow regime at r/d=0.41 for Re=1200, Ri=8.58×10^{-3}, and d=14.5 mm

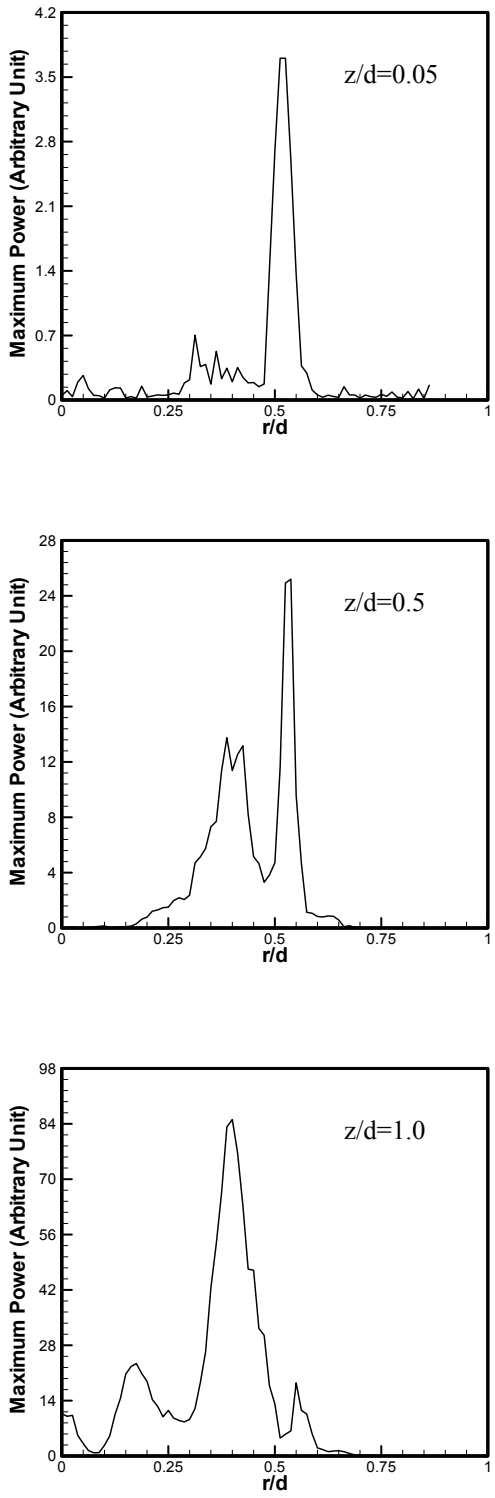

Figure 4. Maximum spectral power at r/d=0.41 for Re=1200, Ri=8.58x10^{-3}, and d=14.5 mm

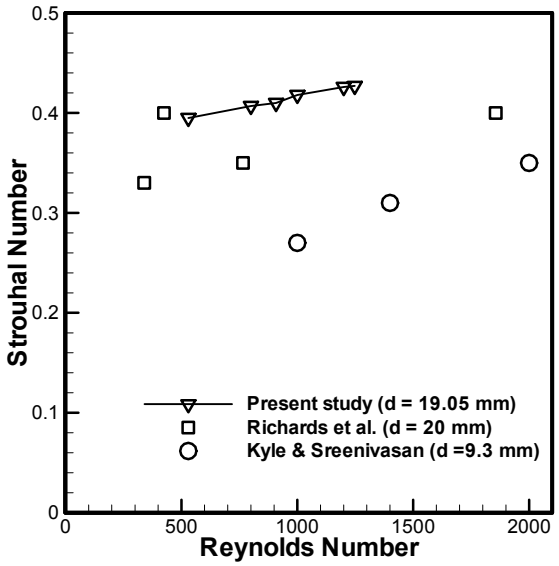

Figure 5. Strouhal number versus Reynolds number for a fixed tube diameter

(a)

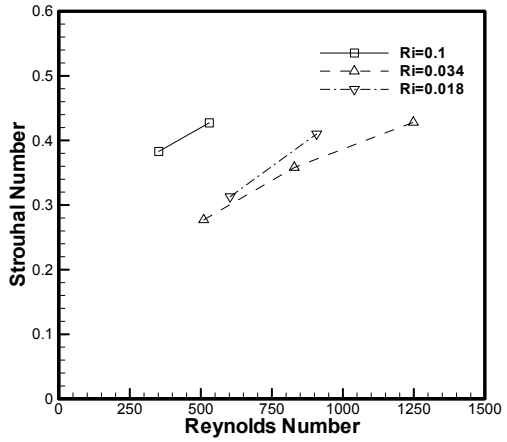

(b)

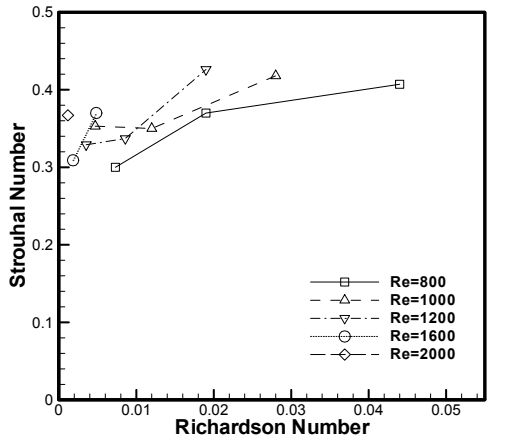

Figure 6 (a) Strouhal number versus Reynolds number, (b) Strouhal number versus Richardson number

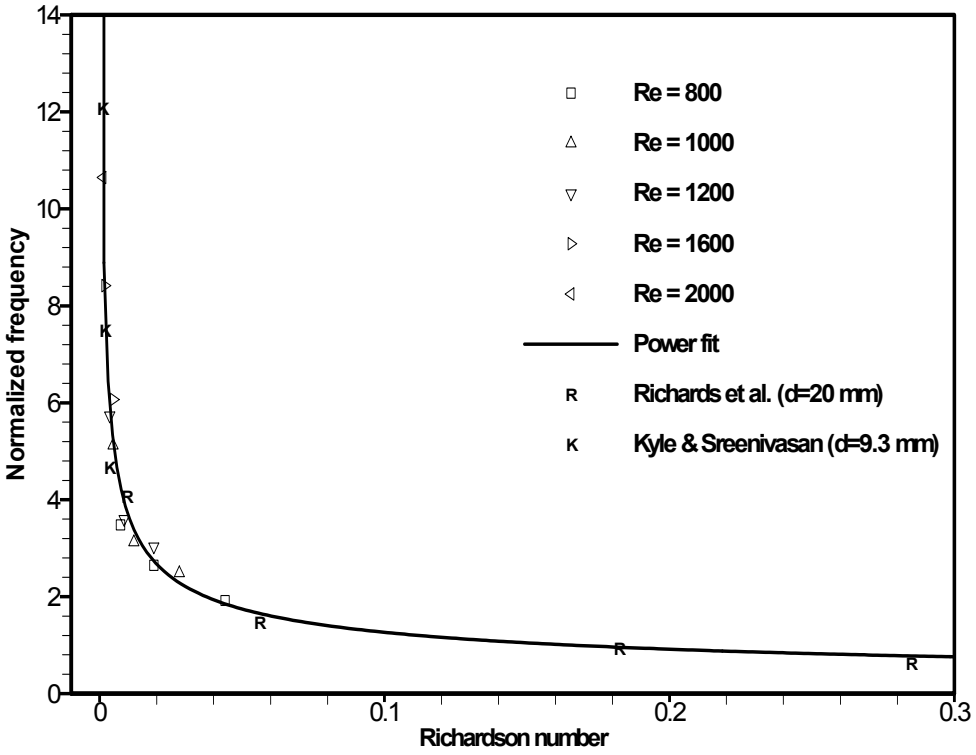

Figure 7. Flow oscillation frequency versus Richardson number for fixed Reynolds numbers

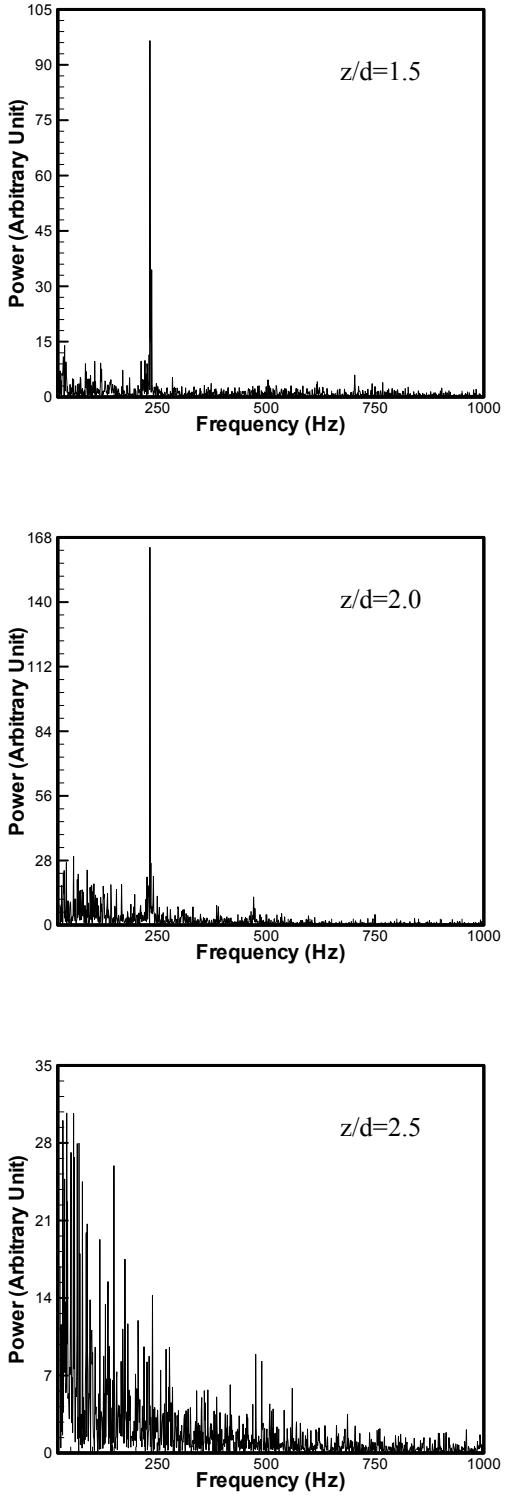

Figure 8. Power spectra in the transitional/turbulent flow regime at r/d=0.41 for Re=1200, $Ri=8.58x10^{-3}$, and d=14.5 mm

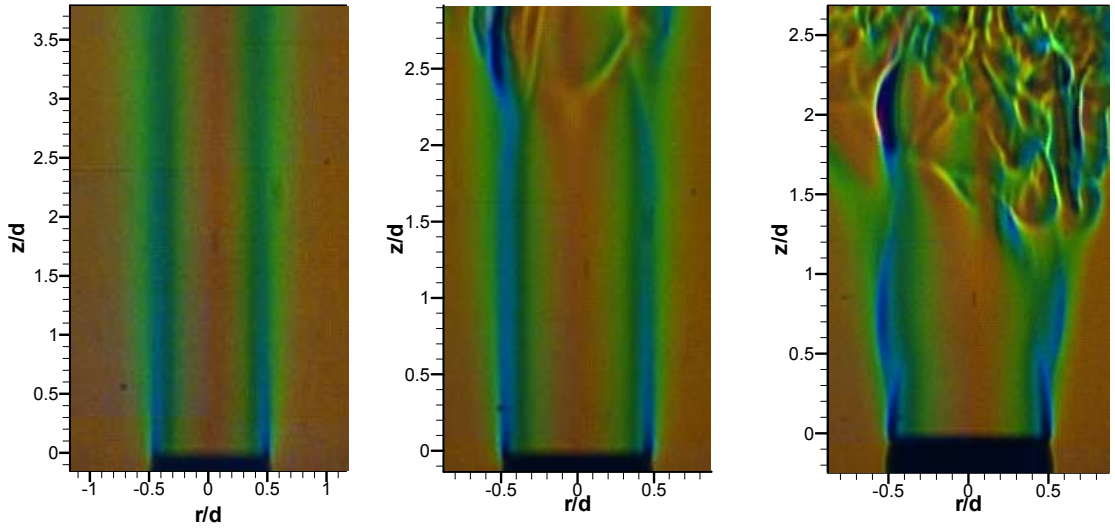

Ri=18x10^{-3}
Re=510

Ri=18x10^{-3}
Re=830

Ri=18x10^{-3}
Re=1250

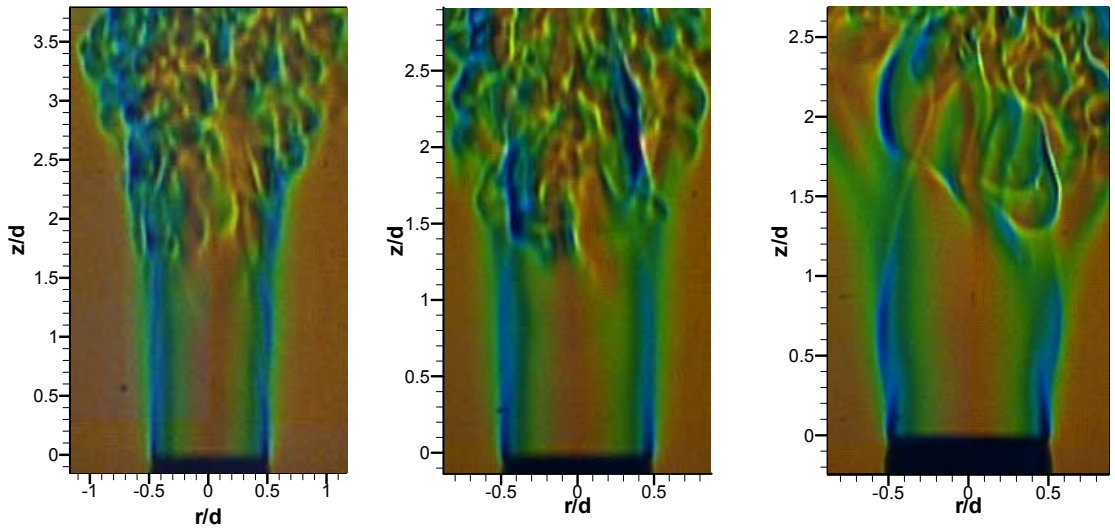

Re=1200
Ri=3.53x10^{-3}

Re=1200
Ri=8.58x10^{-3}

Re=1200
Ri=19x10^{-3}

Figure 9. Effect of Reynolds number and Richardson number on transition from laminar to turbulent flow

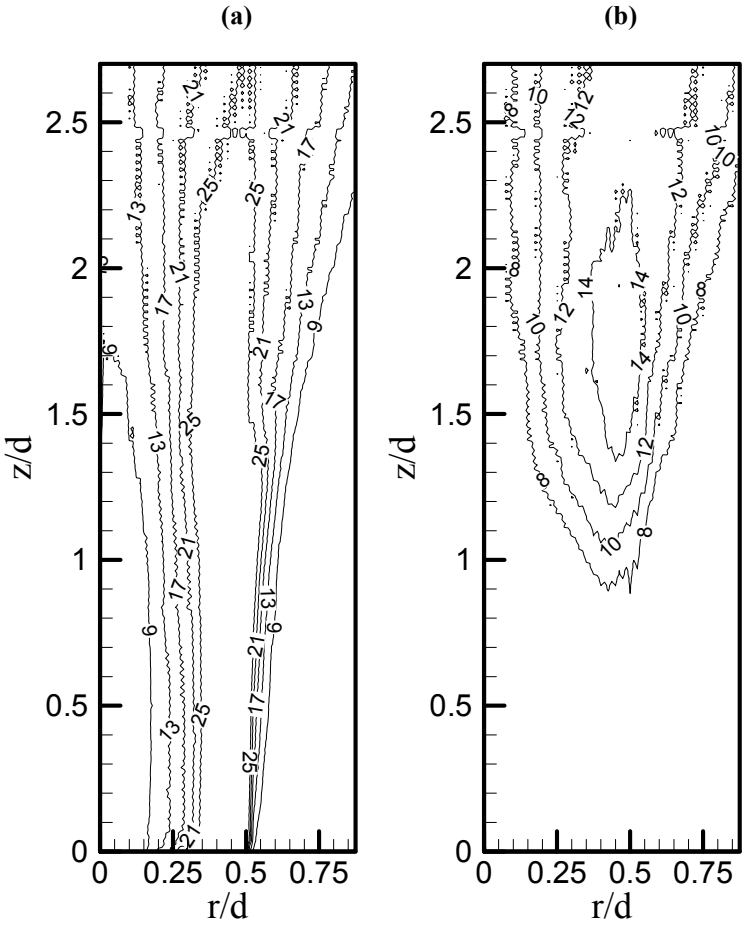

Figure 10. Mean and rms angular deflection for Re=1600, Ri=4.83x10^{-3}, and d=14.5 mm, (a) mean angular deflection (b) rms angular deflection; Contour levels are in milli degrees

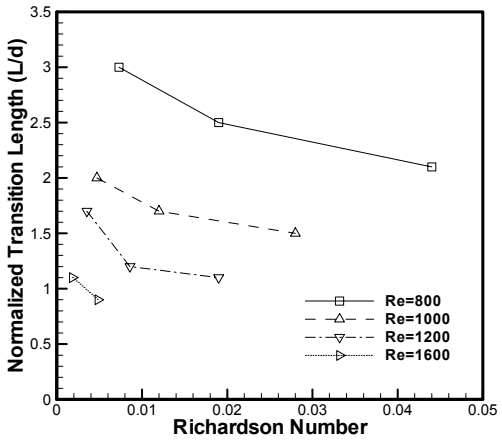

Figure 11. Normalized flow transition length versus Richardson number for fixed Reynolds numbers

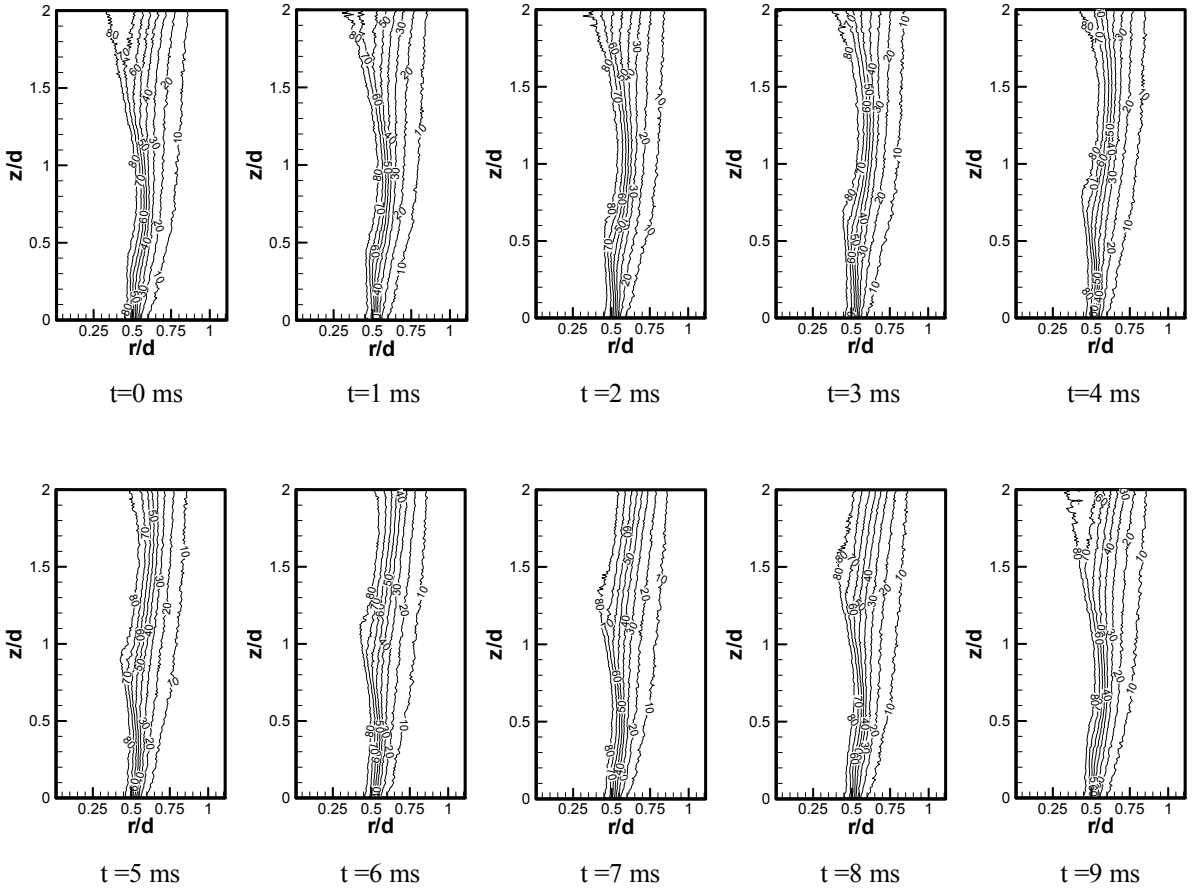

Figure 12. Instantaneous helium mole percentage contours during an oscillation cycle for Re=800, Ri=4.4x10^{-2}, and d=19.05 mm

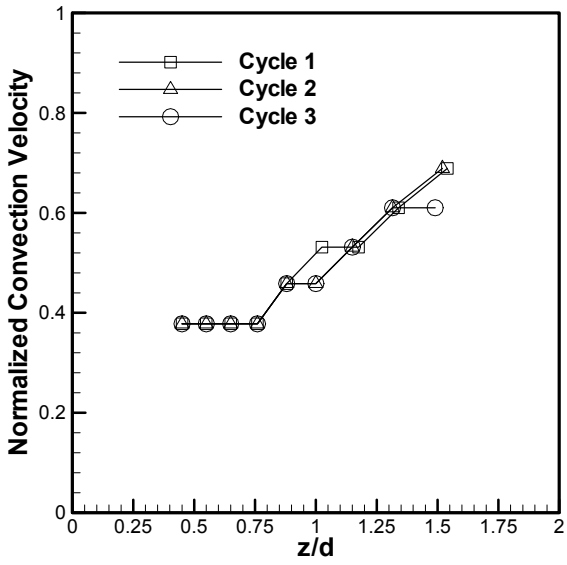

Figure 13. Vortex convection velocity for Re=800, Ri=4.4×10^{-2}, and d=19.05 mm

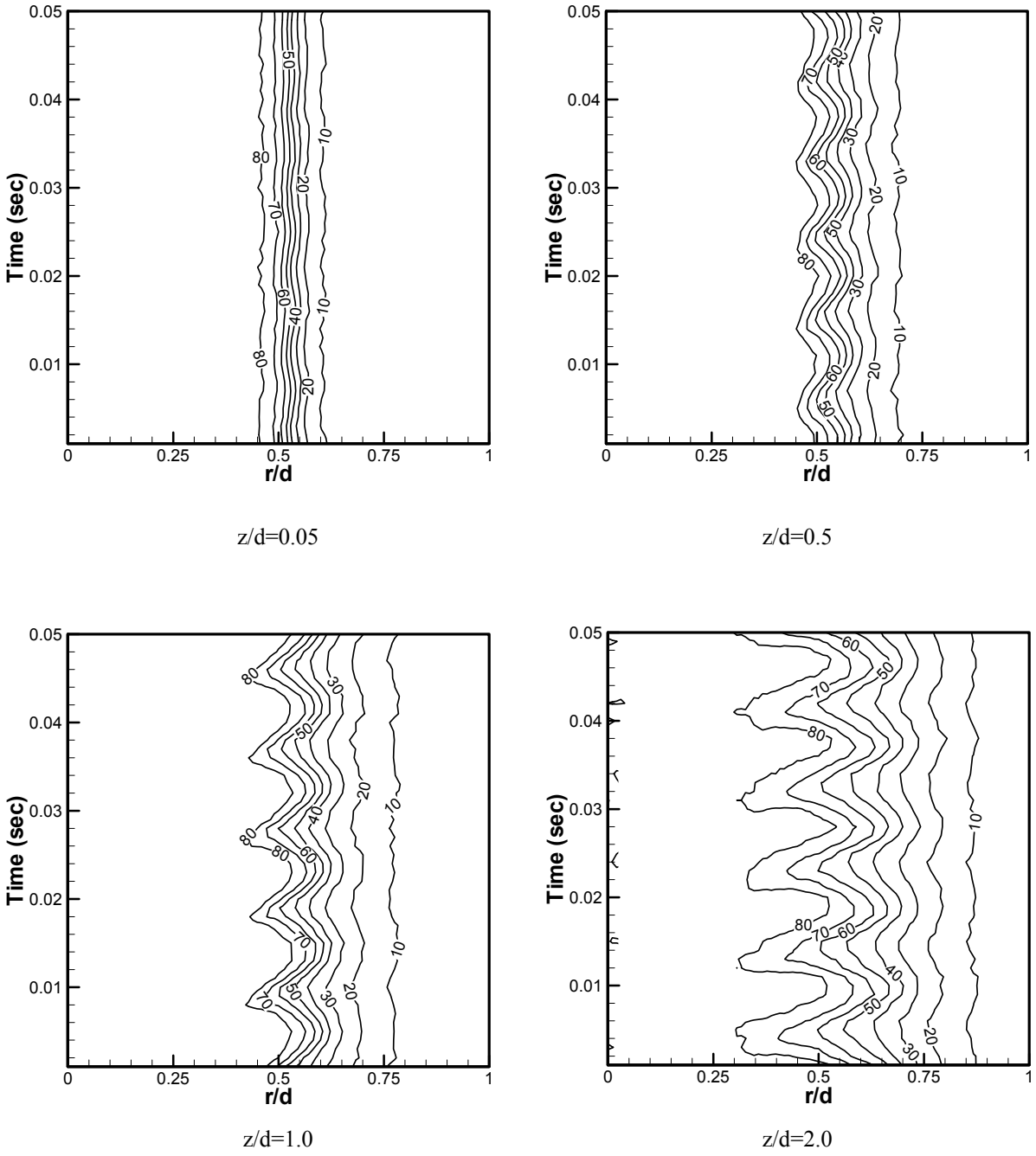

Figure 14. Time-traces of helium mole percentage at different axial planes for Re=800, Ri=4.4×10^{-2}, and d=19.05 mm

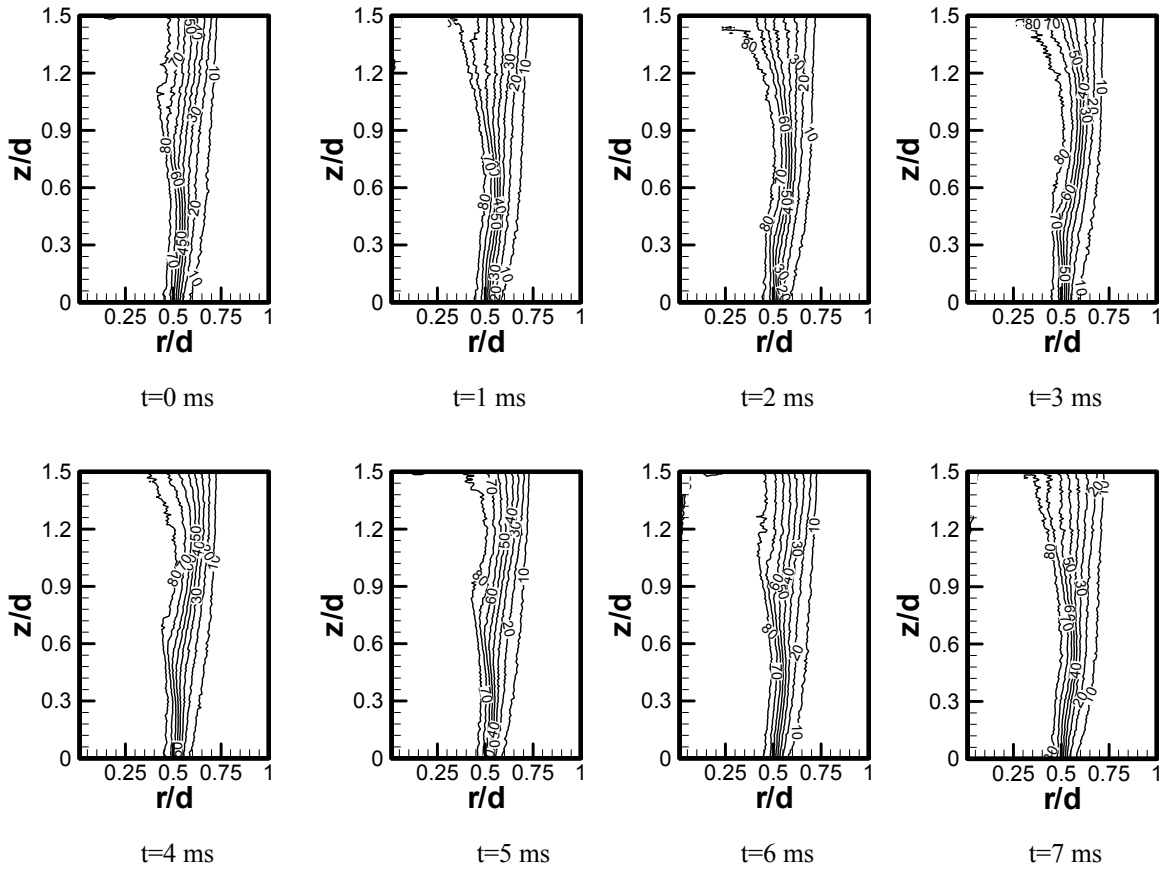

Figure 15. Instantaneous helium mole percentage contours during an oscillation cycle for Re=1200, Ri=1.9x10^{-2}, and d=19.05 mm

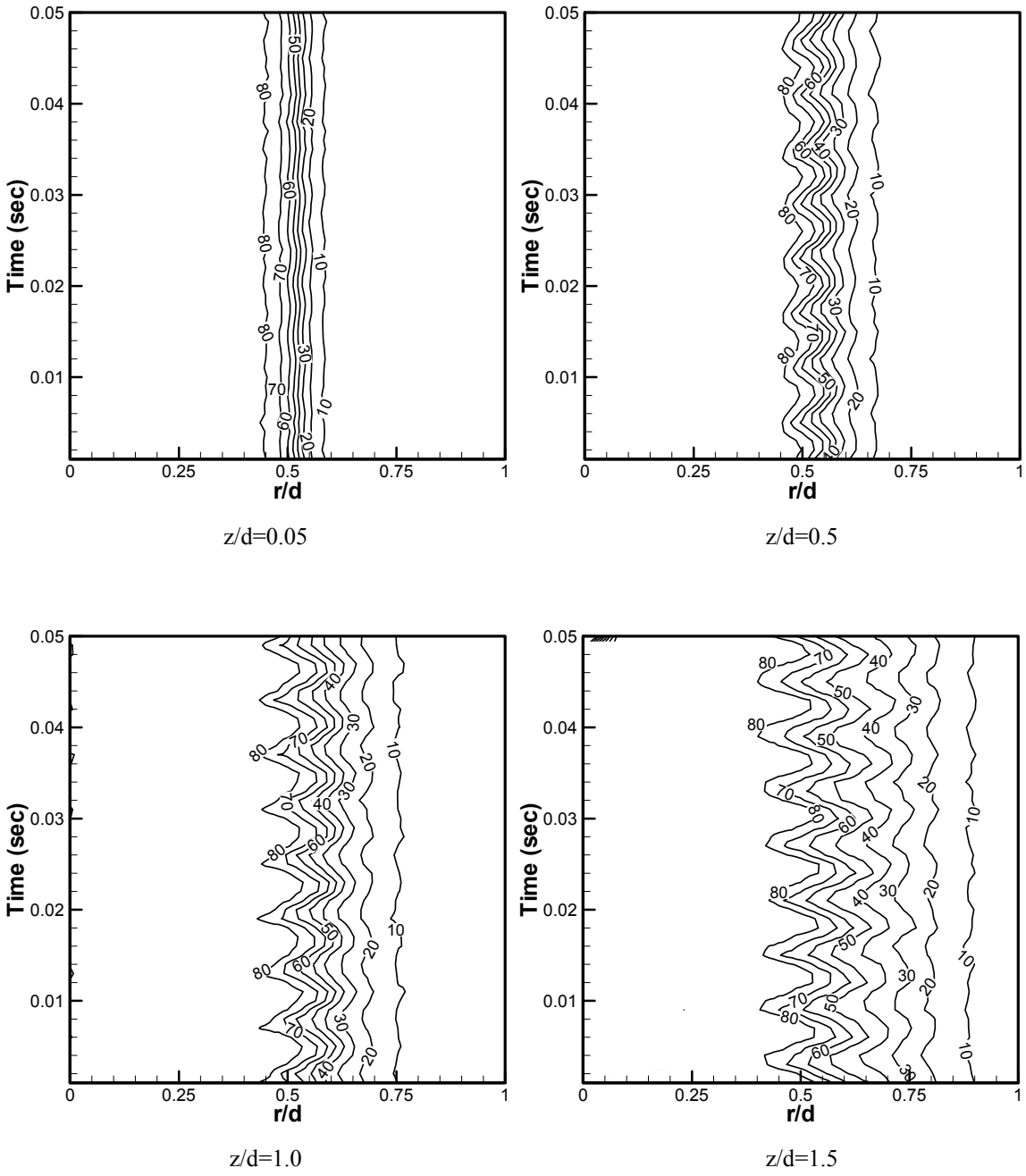

Figure 16. Time-traces of helium mole percentage at different axial planes for Re=1200, Ri=1.9x10^{-2}, and d=19.05 mm

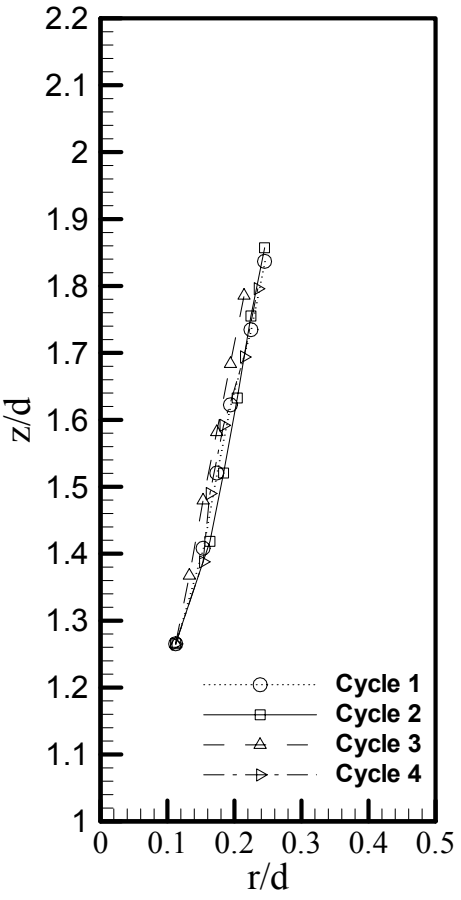

Figure 17. Path of a large scale structure in the transitional/turbulent flow regime for Re=1200, Ri=1.9×10^{-2}, and d=19.05 mm